Supplementary Information

Dynamic localized domains of metallic glasses enable high-capacity SbBi anode for potassium ion batteries

Xi Liu, Xinying Wang, Yang Liu, Ao Jia, Yi Peng, Wanjie Gao, Bingyan Song, Kunming Yang, Jiarui He*, and Yuping Wu

Confucius Energy Storage Lab, School of Energy and Environment & Z Energy Storage Center, Southeast University, Nanjing 211189, PR China.

*Email: hejiarui123@sina.com

Experimental Section

The synthesis of $Cu_2Sb@SbBi_2$:

First, 300 mL of ethanol was mixed with 100 mL of hydrochloric acid (2 mol L^{-1}) and stirred. Then, 0.8 mmol of $SbCl_3$, 0.8 mmol of $BiCl_3$, and 0.8 mmol of $CuSO_4$ were added to the solution, stirred for 30 min, and 32 mmol of Fe powder was added after complete dissolution. After standing for 6 h, the reaction was washed three times with ethanol and water filtration, respectively, and then freeze-dried in a vacuum for 24 h. Finally, the $Cu_2Sb@SbBi_2$ powder was collected.

The synthesis of Cu_2Sb:

Synthesis with $Cu_2Sb@SbBi_2$ is similar to that of Cu_2Sb, merely requiring that $SbCl_3$ be changed to 0.8 mmol and $CuSO_4$ to 1.6 mmol, with Fe still in excess.

The synthesis of $SbBi_2$:

Synthesis with $Cu_2Sb@SbBi_2$ is similar to that of Cu_2Sb, merely requiring that $SbCl_3$ be changed to 0.8 mmol and $BiCl_3$to 1.6 mmol, with Fe still in excess.

Characterizations. The morphologies and microstructures of the samples were analysed by field emission scanning electron microscope (SEM, Zeiss, Sigma 360) and Transmission electron microscopy (TEM, FEI Talos F200X G2). The crystal structure of the samples was identified by powder X-ray diffraction (Dandong Haoyuan Analytical DH7006B) using Cu K_α radiation. Raman scattering was performed on an alpha300 Access microscope equipped with a 532 nm laser as the excitation source at

room temperature. Brunauer Emmett Teller (iPore400, PhysiChem Instruments, China.) method was utilized to calculate the specific surface areas and the pore size distributions.

The Preparation of Electrodes and Cell Assembly. The active material ($Cu_2Sb@SbBi_2$, Cu_2Sb and $SbBi_2$), acetylene black, and Polyacrylic Acid (PAA) binder were mixed with a mass ratio of 7:2:1 to form a homogeneous slurry, and then the slurry was spread on the rough side of copper foil and dried at 80 ^oC under vacuum for 12 hours. Afterward, the dried material was cut into a 0.785 cm^2 (Diameter =1.0 cm) disk and pressed with 4.0 MPa to get the electrodes. Here, the mass loading of active material was about 1.0 ± 0.2 mg cm^{-2}. Preliminary cell tests were done with 2032 coin-type cells, which were fabricated in an argon-filled glove box, where potassium metal as the counter electrode a Whatman GF/D glass fiber as separator, and 4.0 mol L^{-1} potassium bis(fluorosulfonyl)imide (KFSI) dissolved in dimethoxyethane (DME) was used as the electrolyte.

Materials Characterizations

The morphologies and microstructures of the samples were analysed by field emission scanning electron microscope (SEM, Hitachi SU8010) and Transmission electron microscopy (TEM, FEI Tecnai G20). The crystal structure of the samples was identified by powder X-ray diffraction (XRD) (Rigaku D/Max-III diffractometer) using Cu K_α radiation and the diffraction angle was stepped with a scan rate of 8^o min^{-1}. Raman scattering was performed on a Horiba Jobin Yvon confocal Raman microscope equipped with a 532 nm laser as the excitation source at room temperature. Brunauer

Emmett Teller (iPore400, PhysiChem Instruments, China.) method was utilized to calculate the specific surface areas and the pore size distributions.

Electrochemical measurements

The charge-discharge performance and GITT measurements of the cells were tested on a NEWARE Battery Test System (Shenzhen, China). The GITT method was performed by testing a series of pulse current density of 0.1 A g^{-1} for 10 min, followed by a relaxation interval of 60 min for each pulse. Cyclic voltammetry (CV) and electrochemical impedance spectroscopy (EIS) measurements (amplitude, 5 mV; frequency, 0.01 Hz to 100 kHz) were conducted on an electrochemical workstation (DongHua Analytical DH7006B).

Statistical Analysis

The charge-discharge performance and GITT measurements of the cells were tested on a LAND CT2001A battery tester (Wuhan, China) and NEWARE Battery Test System (Shenzhen, China). EIS and CV measurements were conducted on an electrochemical workstation (DongHua Analytical DH7006B. The above data are obtained by direct testing, for the processing of the data obtained has been described in the manuscript and supporting information, and the processing software is used for commercial Origin and PowerPoint processing.

Calculation of ion diffusion coefficient using GITT.

The calculation of the ion diffusion coefficient based on the galvanostatic intermittent titration technique (GITT) uses the following equation:

$$D_{K^+} = \frac{4}{\pi\tau}\left(\frac{nV_m}{A}\right)^2\left\{\frac{\Delta E_S}{\Delta_{E\tau}}\right\}^2, t \ll L^2/D_{K^+}$$

Where, τ is the relaxation time (also known as pulse time), n is the molarity of the active substance, V_m is the molar volume, and A is the contact area (cm^{-2}) of the electrode/electrolyte, ΔE_s is the voltage change due to the pulse (V); ΔE_τ is the voltage change due to the constant current charge (discharge) (V), L is the diffusion length (cm).

DFT Calculation Details.

All the DFT calculations in the article were performed by the Vienna Ab initio Simulation Package (VASP)[1]. In the calculations, the projector augmented wave (PAW)[2] method was performed, and the generalized gradient approximation (GGA) of Perdew-Burke-Ernzerhof (PBE)[3] functional was used for the exchange-functional, the energy cutoff for the plane wave basis expansion is setted to be 500eV, the Brillouin zone integration was sampled by 2*2*1 for the geometry optimization and scf calculations, then the force on each atom less than 0.03 eV/Å was set for convergence criterion of geometry relaxation[4]. To avoid the interaction between periodic structures,15 Å vacuum was added along the z direction. The self-consistent calculations apply a convergence energy threshold of 10^{-5} eV and the DFT-D3 method was employed to consider the van der Waals interaction [5]. The adsorption energy of K^+ was calculated according to

$E_{ads} = E_{total} - E_{sub} - E_K$

where E_{total} is the total energy of the K^+ adsorbed systems, E_{sub} and E_K are the energies of the substrate and the isolated molecule or K^+, respectively.

References

[1] Kresse, G.; Furthmüller, J. Comp Mater Sci 1996, 6, (1), 15-50.

[2] Blöchl, P. E. Phys. Rev. B 1994, 50, (24), 17953-17979.

[3] Perdew, J. P.; Chevary, J. A.; Vosko, S. H.; Jackson, K. A.; Pederson, M. R.; Singh, D. J.; Fiolhais, C. Phys. Rev. B 1992, 46, (11), 6671-6687.

[4] V. Wang, N. Xu, J.C. Liu, G. Tang, W. T. Geng, VASPKIT: A User-Friendly Interface Facilitating High-Throughput Computing and Analysis Using VASP Code, Computer Physics Communications 267, 108033 (2021).

[5] S. Grimme, J. Antony, S. Ehrlich, H. Krieg, J. Chem. Phys. 2010, 132, 154104.

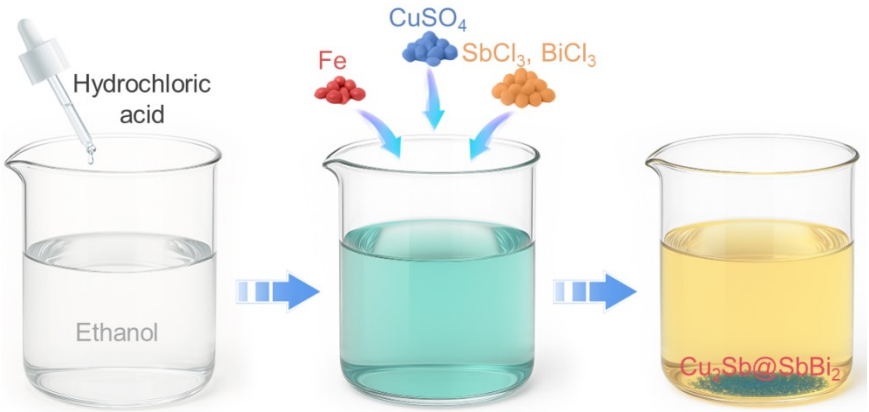

Fig. S1. Synthesis schematic of $Cu_2Sb@SbBi_2$.

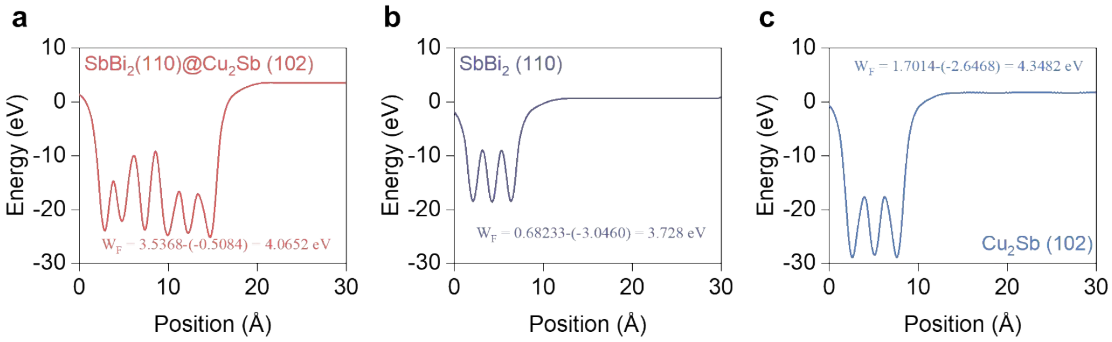

Fig. S2. The work functions of (a) $Cu_2Sb@SbBi_2$, (b) $SbBi_2$, and (c) Cu_2Sb.

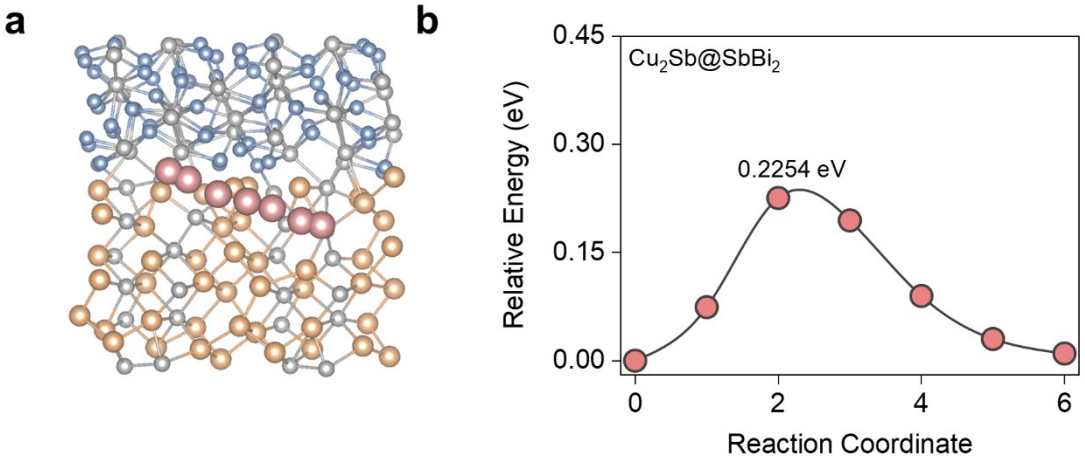

Fig. S3. (a) Atomic structure and (b) diffusion energy barriers of $Cu_2Sb@SbBi_2$ after many cycles.

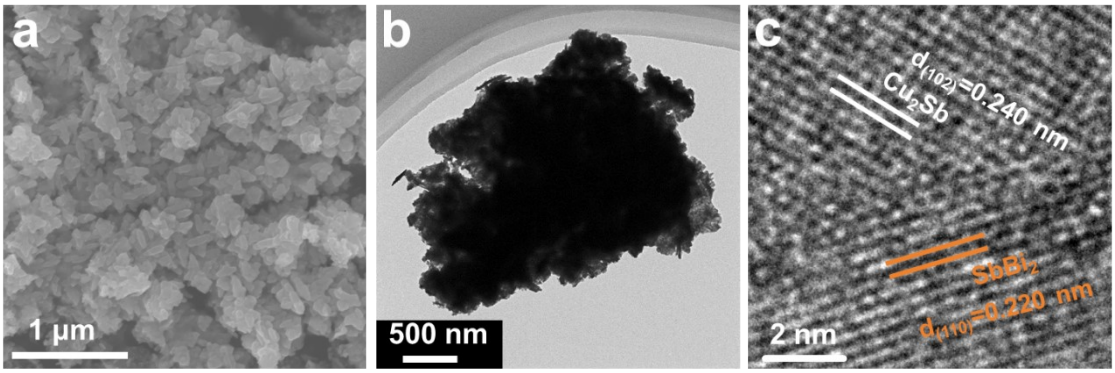

Fig. S4. (a) SEM and (b, c) TEM images of $Cu_2Sb@SbBi_2$.

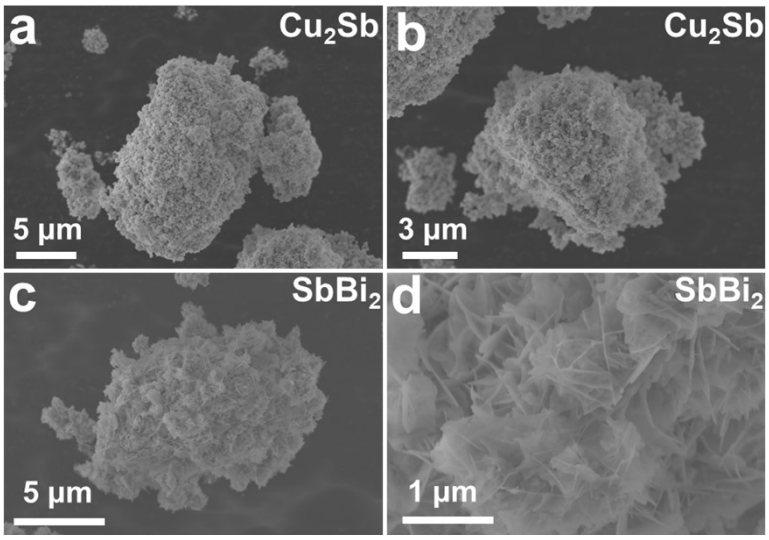

Fig. S5. SEM images of (a-b) Cu_2Sb and (c-d) $SbBi_2$.

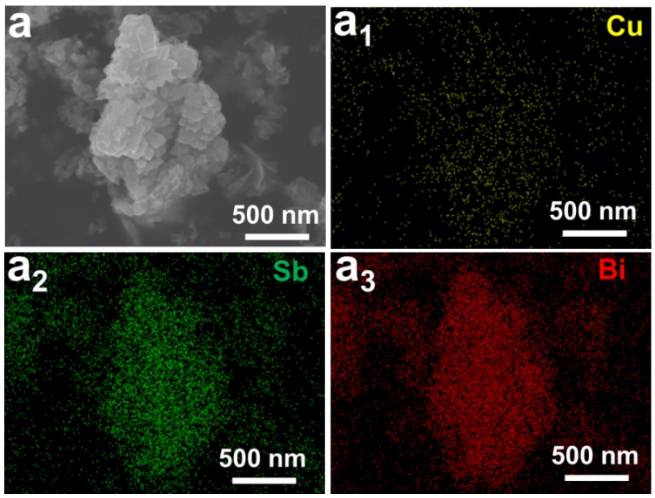

Fig. S6. SEM, Cu, Sb and Bi elemental mapping images of Cu_2Sb@$SbBi_2$.

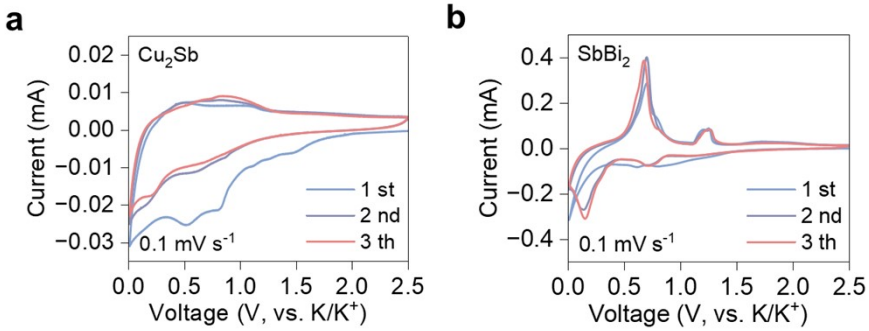

Fig. S7. CV curves of (a) Cu_2Sb and (b) $SbBi_2$ anode.

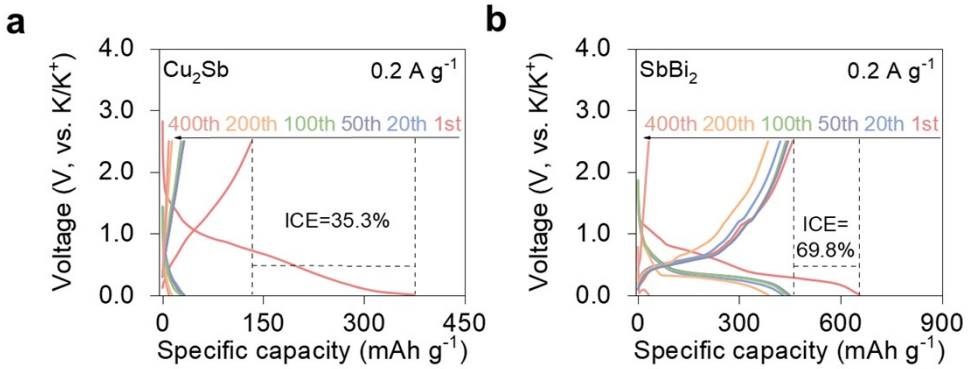

Fig. S8. GCD curves at 0.2 A g^{-1} of (a) Cu_2Sb and (b) $SbBi_2$.

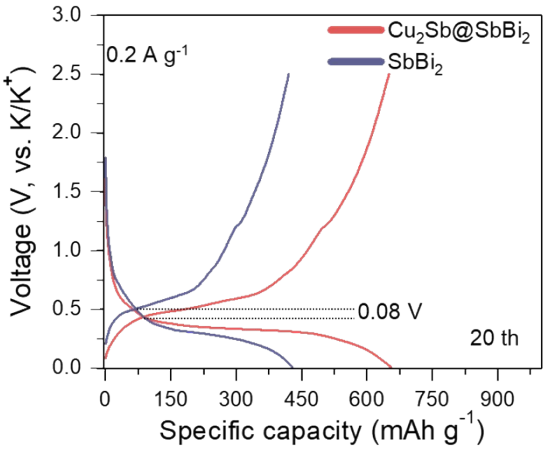

Fig. S9. GCD curves of (a) Cu_2Sb@ $SbBi_2$ and (b) $SbBi_2$ at 0.2 A g^{-1} with the 20th cycles.

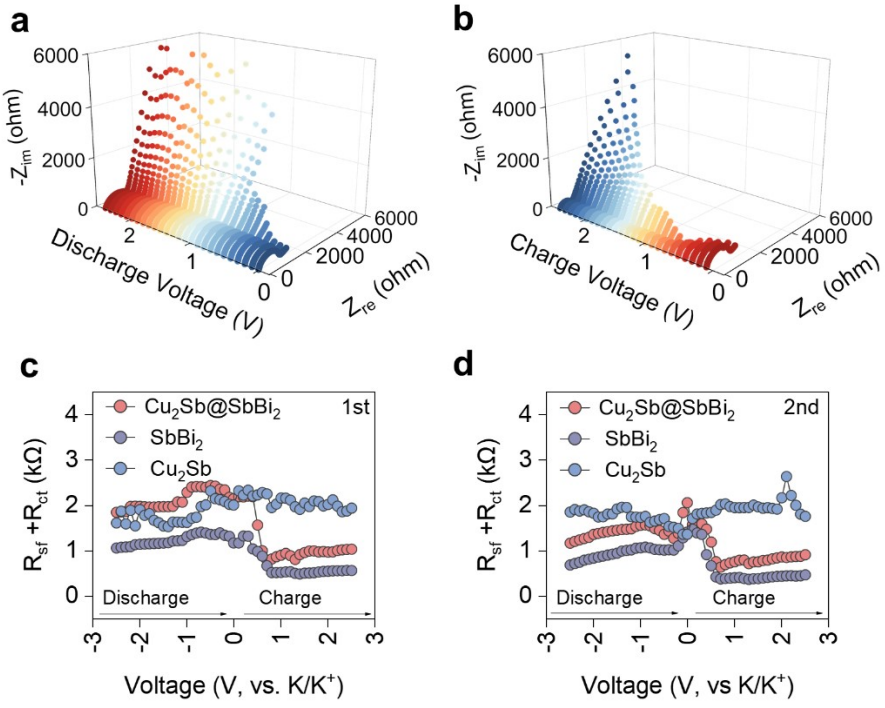

Fig. S10. *In-situ* EIS at different potentials at 1st (a) discharge, (b) charge of Cu_2Sb@$SbBi_2$ at 0.1 A g^{-1}. (c) *In-situ* EIS at different potentials the 1st, and (d) 2nd for impedance R_{sf} + R_{ct} value of Cu_2Sb@$SbBi_2$, $SbBi_2$, and Cu_2Sb at 0.1 A g^{-1}.

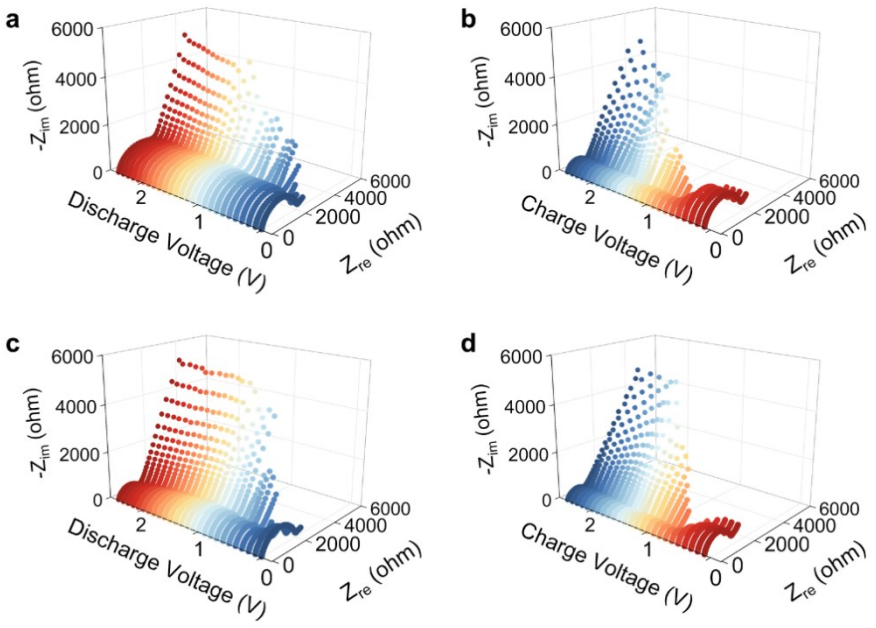

Fig. S11. *In-situ* EIS at different potentials at 1st (a) discharge, (b) charge, at 2nd (c) discharge, (d) charge of $SbBi_2$ at 0.1 A g^{-1}.

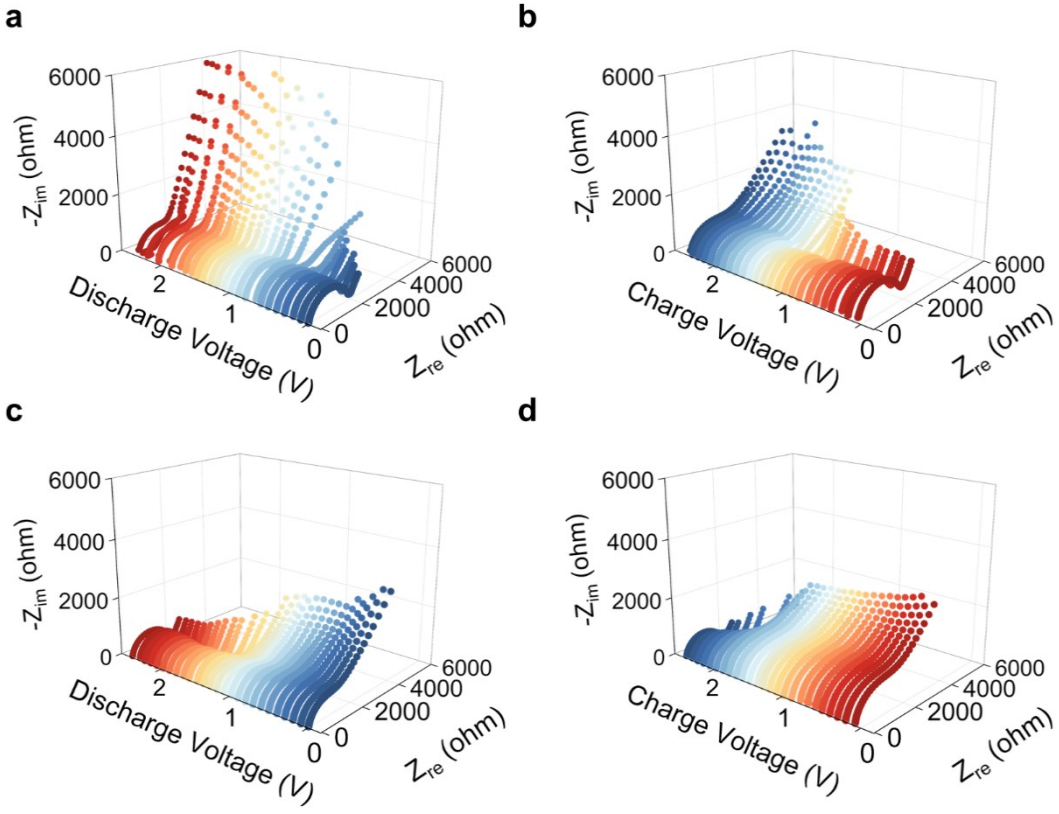

Fig. S12. *In-situ* EIS at different potentials at 1st (a) discharge, (b) charge, 2nd (c)

discharge, (d) charge of Cu_2Sb at 0.1 A g^{-1}.

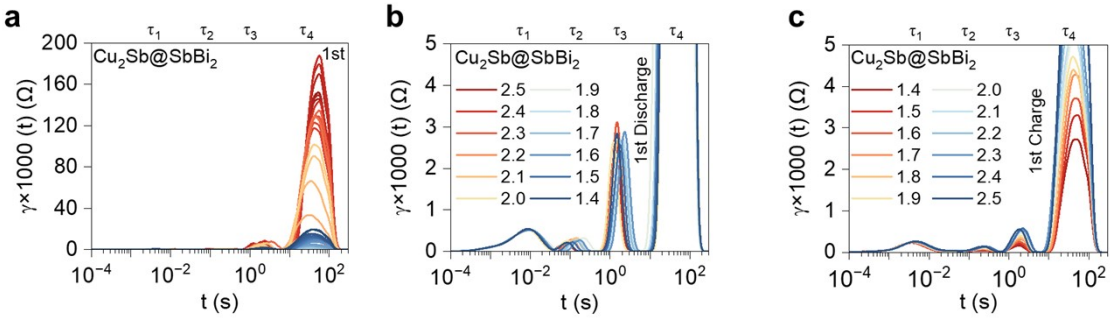

Fig. S13. (a-c) *In-situ* different potential DRT data of Cu_2Sb@$SbBi_2$ at the first cycle.

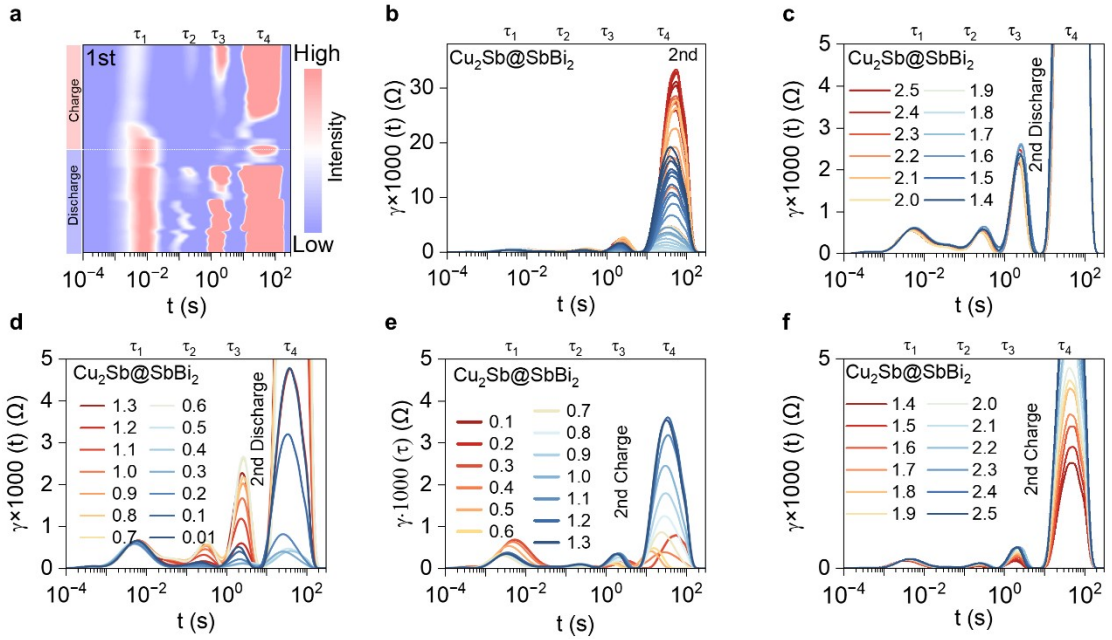

Fig. S14. *In-situ* EIS at different potentials for DRT data of Cu_2Sb@$SbBi_2$ at the (a) 1st and (b-f) 2nd cycle at 0.1 A g^{-1}.

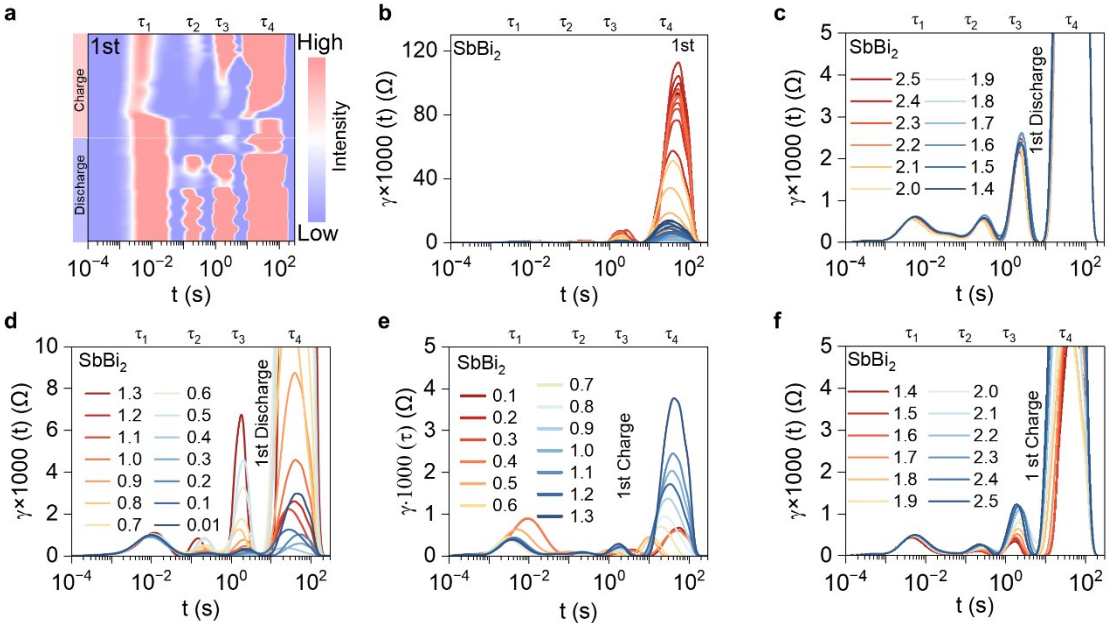

Fig. S15. *In-situ* EIS at different potentials for DRT data of $SbBi_2$ at the first cycle at 0.1 A g^{-1}.

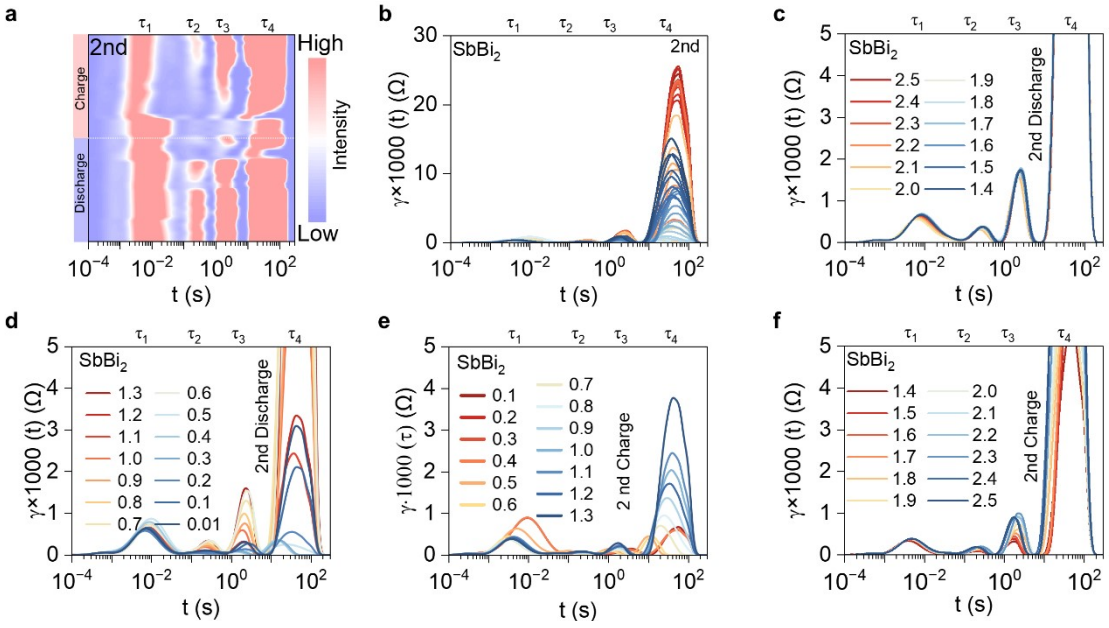

Fig. S16. *In-situ* EIS at different potentials for DRT data of $SbBi_2$ at the 2nd cycle at 0.1 A g^{-1}.

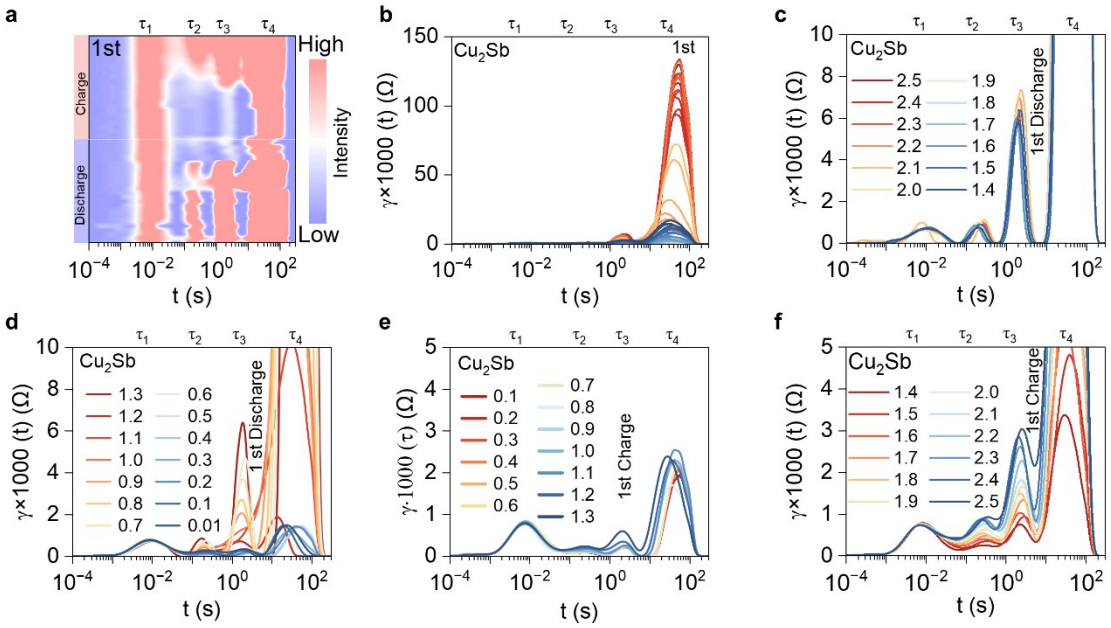

Fig. S17. *In-situ* EIS at different potentials for DRT data of Cu_2Sb at the first cycle at 0.1 A g^{-1}.

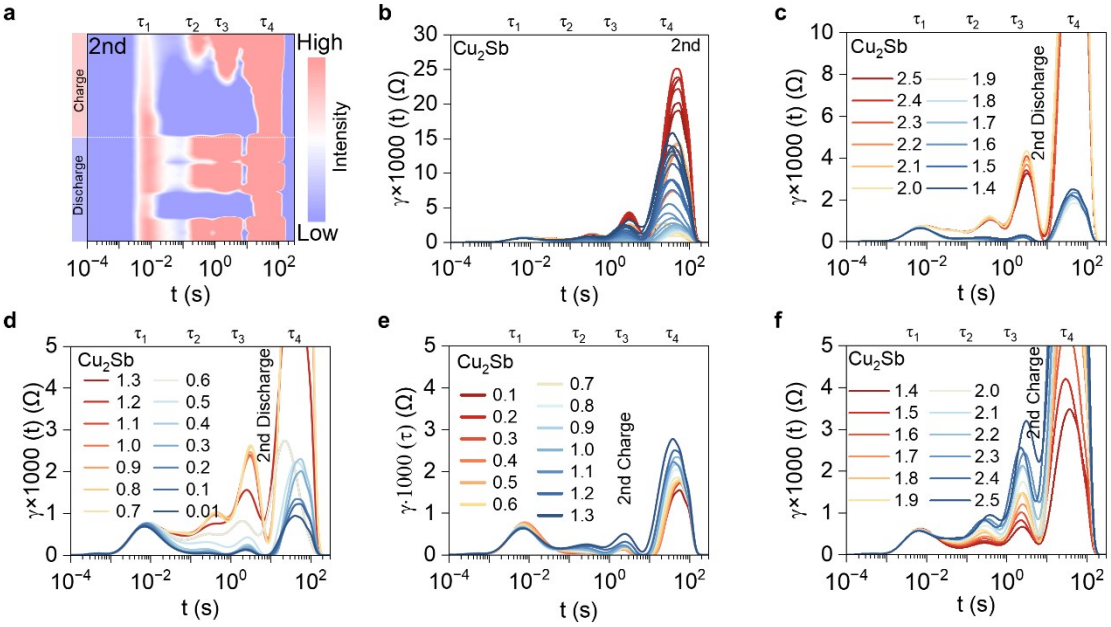

Fig. S18. *In-situ* EIS at different potentials for DRT data of Cu_2Sb at the 2nd cycle at 0.1 A g^{-1}.

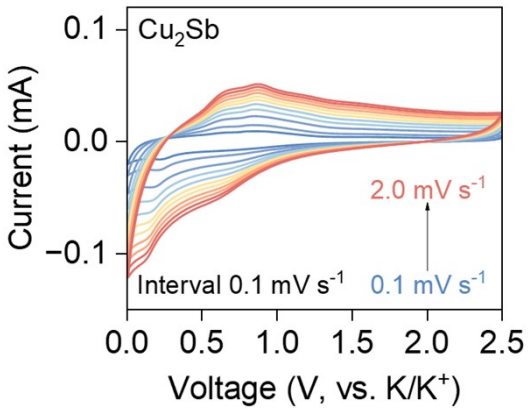

Fig. S19. CV curves at different scan rates of Cu_2Sb anode.

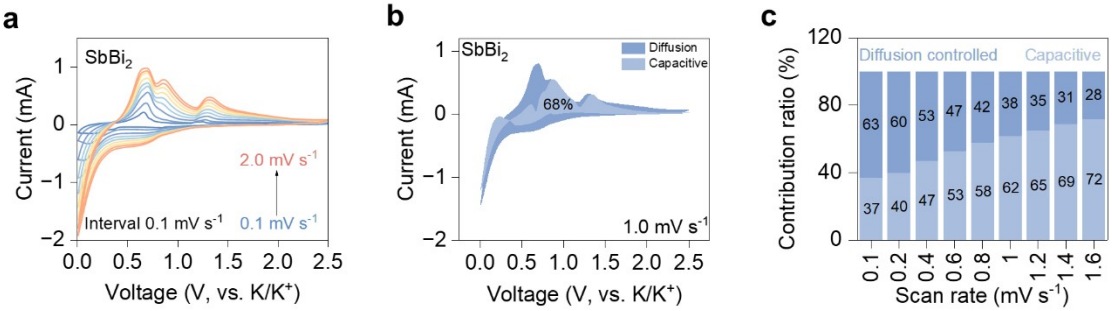

Fig. S20. (a) CV curves at different scan rates, capacity contribution of samples (b) at the scan rate of 1.2 mV s^{-1} of $SbBi_2$ anode. (c) Capacity contribution of samples at different scan rates of $SbBi_2$.

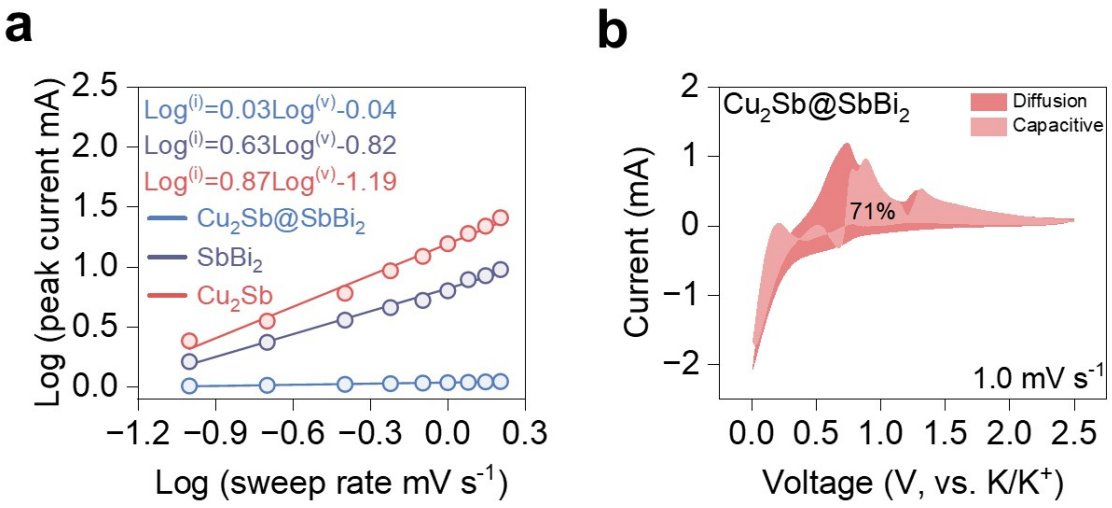

Fig. S21. (a) The slope of the $log^{(v)}$-$log^{(i)}$ image of $Cu_2Sb@SbBi_2$, Cu_2Sb, and $SbBi_2$. Capacity contribution of samples (b) at the scan rate of 1.2 mV s^{-1} of $Cu_2Sb@SbBi_2$.

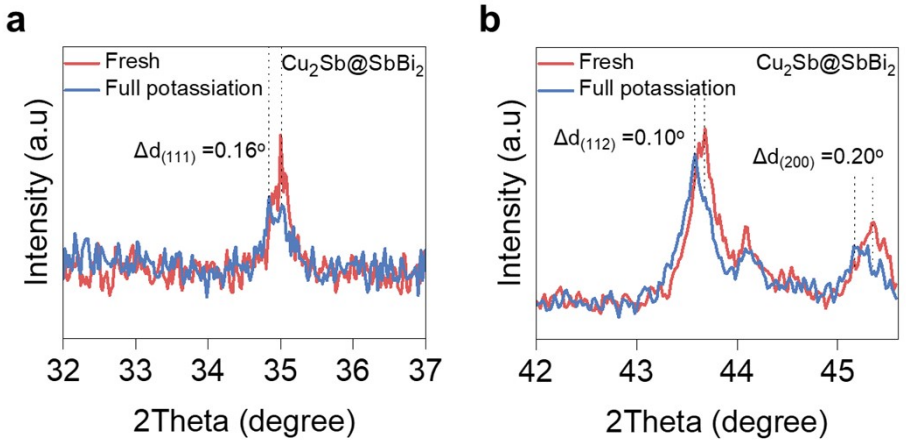

Fig. S22. The XRD enlargement of (c) (111), (d) (112) and (200) crystal surfaces of Cu_2Sb.

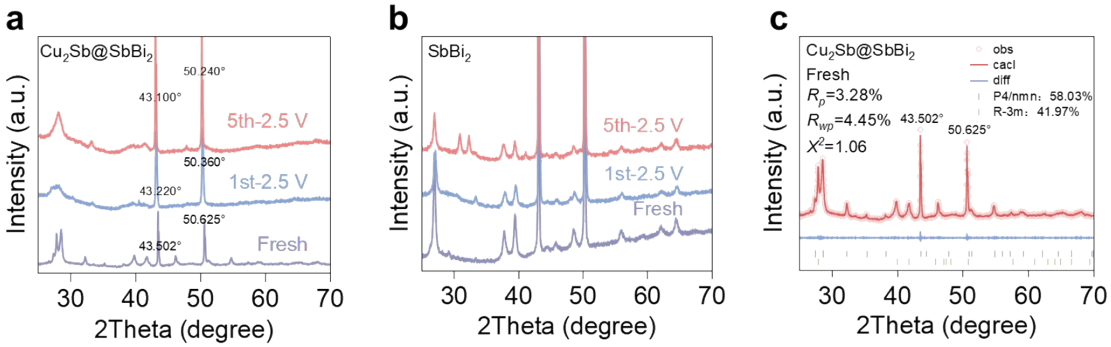

Fig. S23. XRD comparison of (a) $Cu_2Sb@SbBi_2$ and (b) $SbBi_2$ in different states. (c) Rietveld refinement of powder XRD data of $Cu_2Sb@SbBi_2$ at the fresh state.

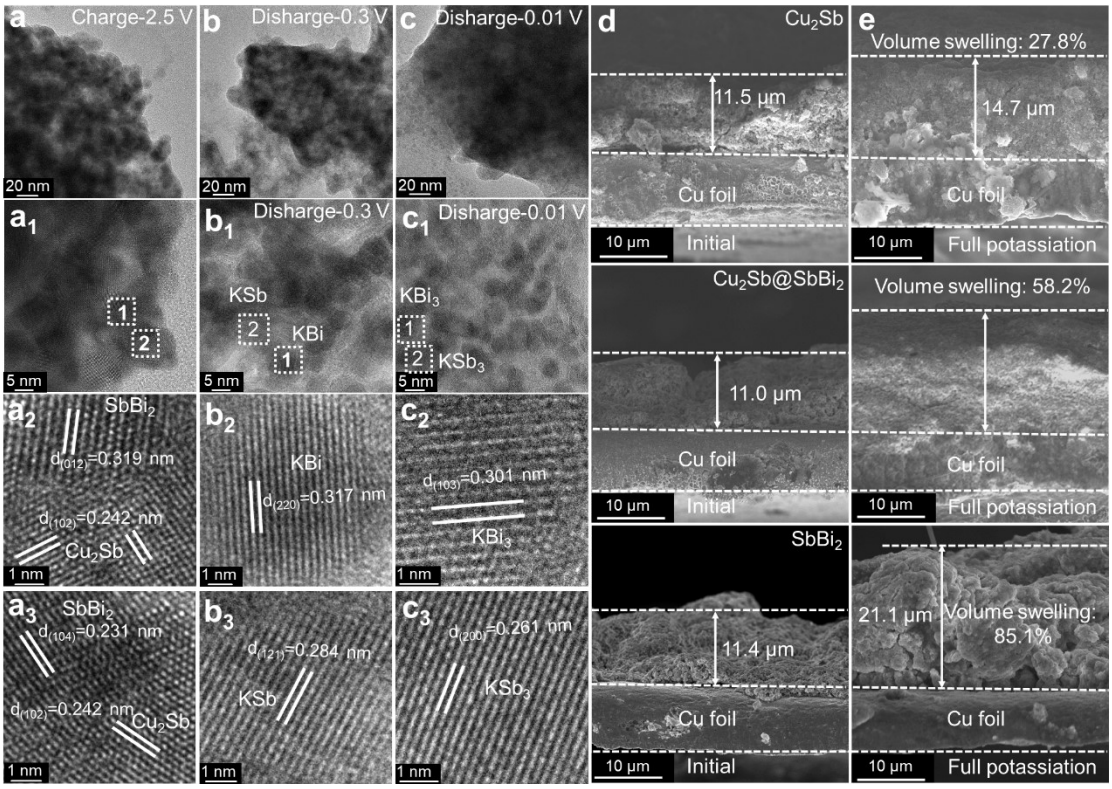

Figure S24. The potassium storage mechanism of $Cu_2Sb@SbBi_2$ anode. *Ex-situ* TEM images of $Cu_2Sb@SbBi_2$ when charged to (a) 2.5 V, discharged to (b) 0.3 V, and (c) 0.01 V. (d-e) Cross-sectional SEM images of Cu_2Sb, $Cu_2Sb@SbBi_2$, and $SbBi_2$.

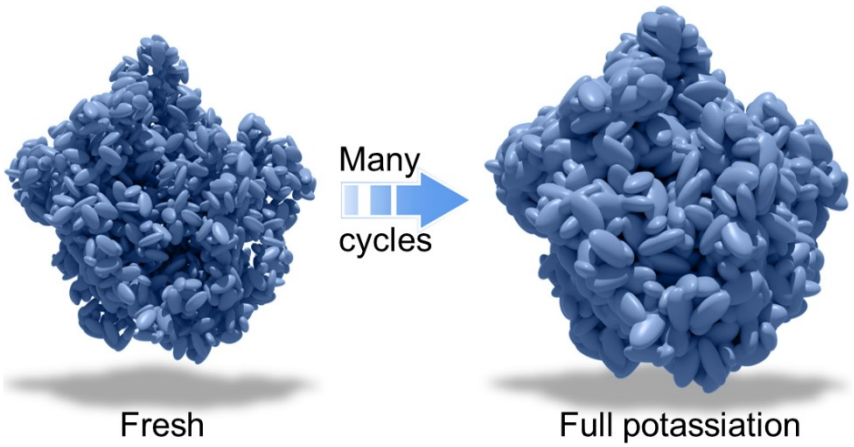

Fig. S25. Schematic illustration of the potassium storage mechanism in the $Cu_2Sb@SbBi_2$ anode.

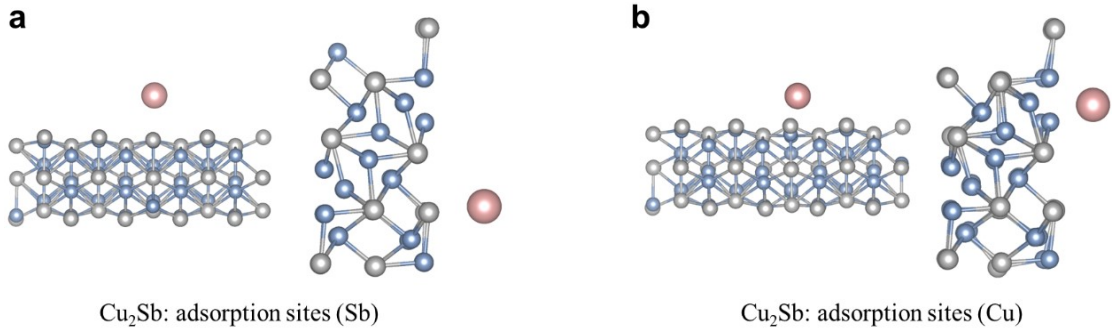

Fig. S26. Structural model of the adsorption of K-ions by (a) Sb and (b) Cu atoms in Cu_2Sb.

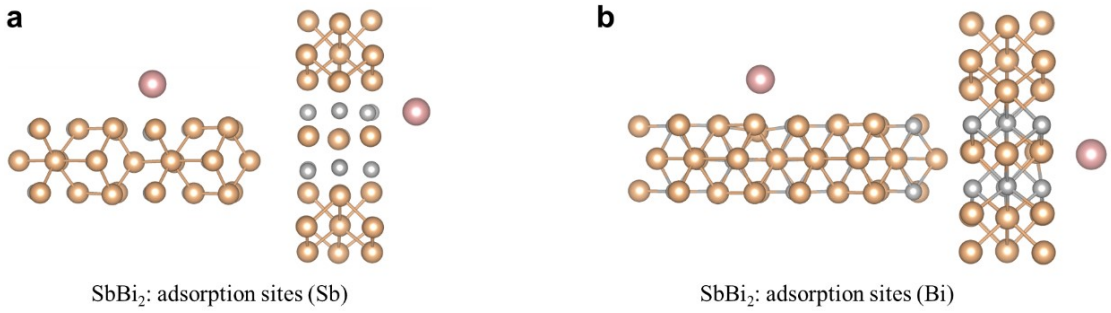

Fig. S27. Structural model of the adsorption of K-ions by (a) Sb and (b) Bi atoms in $SbBi_2$.

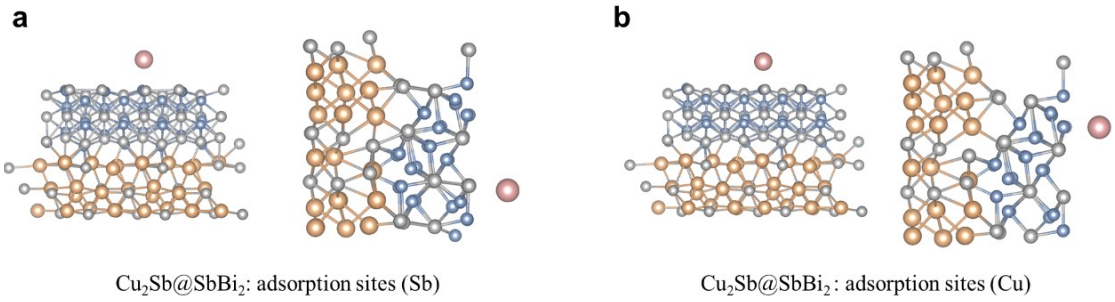

Fig. S28. Structural model of the adsorption of K-ions by (a) Sb and (b) Cu atoms in $Cu_2Sb@SbBi_2$.

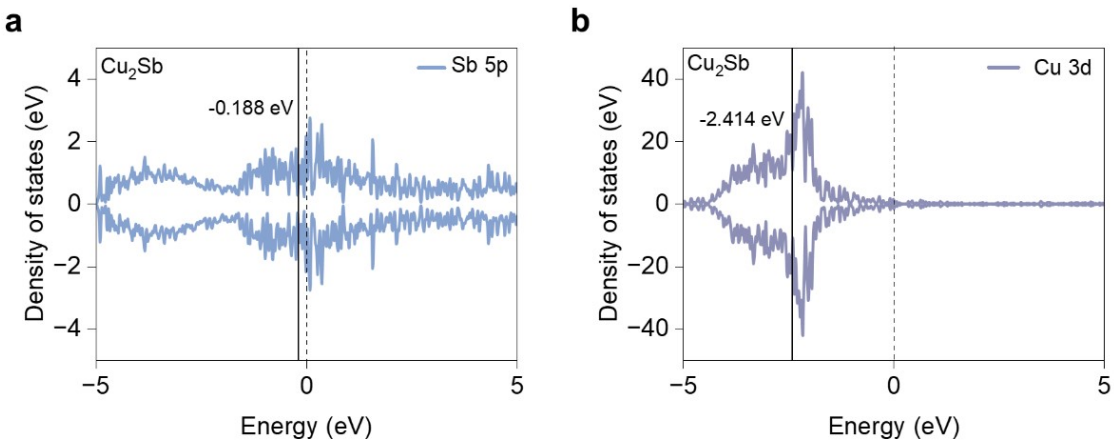

Fig. S29. The (a) p-band center of Sb and (b) d-band center of Cu for Cu_2Sb.

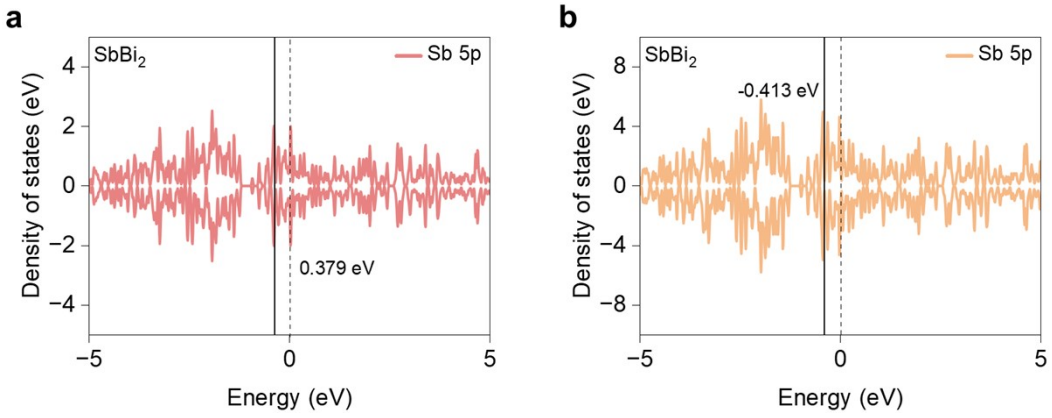

Fig. S30. The (a) p-band center of Sb and (b) Bi for $SbBi_2$.

Table S1. Electrochemical performance comparison with some reported representative Sb-based anodes in PIBs.

Materials	Preparation method	Percentage of active materials (wt%)	The proportion of active materials, conductive additives, and binder	Active materials content in the whole electrode (wt%)	Cycling performance (mA h g^{-1}) (Based on the whole electrode)	Initial reversible capacity (mAh/g)	ICE	Refs
2D-$Sb_{0.6}Bi_{0.4}$	One-step substitution	100%	7: 2: 1	70%	~399/0.2 A g^{-1}/400th	433.7/0.2 A g^{-1}	68%	S1[1]
BiSb-HTR	High-temperature radiation	81.5%	8: 1: 1	65.2%	325/0.2 A g^{-1}/800th	407.8/0.2 A g^{-1}	~66.1 %	S[2]
$Bi_{0.67}Sb_{1.33}S_3$/PET@PTA	/	73%	7: 2: 1	51.1%	~540/0.2A g^{-1}/rate	~540.0/0.2 A g^{-1}	84%	S3[3]
Sb@$Cu_{15}Si_4$	Direct thermal deposition	/	/	/	~500/0.2A g^{-1}/rate	~500.0/0.2 A g^{-1}	~80%	S4[4]
Sb_2Te_3	hydrothermal	70%	8: 1: 1	80%	308.8/50 mA g^{-1}/100th	292.6/0.2 A g^{-1}	60%	S5[5]
M-BiSnSb	Equilibrium tube furnace calcination	66.7%	8: 1: 1	53.4%	~500/0.2 A g^{-1}/400th	384.5/0.2 A g^{-1}	58.9%	S6[6]
BiSbO	hydrothermal	100%	7: 2: 1	70%	368.5/50 mA g^{-1}/100th	292.5/0.2 A g^{-1}	57.4%	S7[7]
Sb_2Se_3	carbonizing	51.3%	7: 2: 1	36%	423 /0.1 A g^{-1}/100th	439/0.2 A g^{-1}	65%	S8[8]
$Sb_{0.25}Bi_{0.75}$@NC		75%	7: 2: 1	52.5%	301.9/0.1 A g^{-1}/500th	424.7/0.2 A g^{-1}	45%	S9[9]
Cu_2Sb@$SbBi_2$	**One-step substitution**	**100%**	**7: 2 : 1**	**70%**	**539/0.2A g^{-1}/400th**	**672/0.2 A g^{-1}**	**84.6%**	**This work**

Note: The specific capacity is calculated based on the total weigh of the whole electrode.

References

[1] X. Liu, X. Wang, Y. Zhou, B. Wang, L. Zhao, H. Zheng, J. Wang, J. Liu, J. Liu, Y. Li, *Adv. Mater.*, **2024**, 36, 2308447.
[2] S. Dou, J. Xu, D. Zhang, W. Liu, C. Zeng, J. Zhang, Z. Liu, H. Wang, Y. Liu, Y. Wang, *Angew. Chem. Int. Ed.,* **2023**, 62, e202303600.
[3] Y. Liu, F. Liu, B. Liu, Y. Xiao, G. Qin, J. Ma, *Angew. Chem. Int. Ed.,* **2023**, 62, e202300599.
[4] S. Imtiaz, N. Kapuria, I. S. Amiinu, A. Sankaran, S. Singh, H. Geaney, T. Kennedy, K. M. Ryan, *Adv. Funct. Mater.*, **2023**, 33, 2209566.
[5] Z. Wang, S. Qiao, M. Ma, T. Li, H. K. Liu, S. X. Dou, S. Chong, *ACS Nano* **2025**, 19, 15148.
[6] S. Dou, Y. Shao, L. Fan, D. Zhang, J. Xu, J. Zhang, H. Tian, Y. B. He, C. Mao, H. Zhu, *Adv. Funct. Mater.*, **2025**, 35, 2412551.
[7] C.-H. Chang, K.-T. Chen, Y.-Y. Hsieh, C.-B. Chang, H.-Y. Tuan, *ACS Nano* **2022**, 16, 1486.
[8] D. Li, H. Liu, J. Li, R. Hou, Y. Li, Z. Sun, L. Wang, W. Han, *Energy Storage Mater.*, **2025**, 104355.
[9] J. Liu, D. Zhang, J. Cui, P. Li, X. Xu, Z. Liu, J. Liu, C. Peng, D. Xue, M. Zhu, *Small* **2023**, 19, 2301444.